



## Segmentation of the Farallon slab

Lijun Liu<sup>\*</sup>, Dave R. Stegman

*Institute of Geophysics and Planetary Physics, Scripps Institution of Oceanography, University of California, San Diego, CA 92093, United States*

### ARTICLE INFO

#### Article history:

Accepted 19 September 2011

Available online 5 October 2011

Editor: Y. Ricard

#### Keywords:

Farallon subduction  
slab segmentation  
seismic tomography  
viscosity  
B&R extension  
toroidal mantle flow

### ABSTRACT

Recent tomography images reveal a complex 3D mantle structure beneath western United States, with feature morphology varying rapidly with depth. By assimilating plate motion history, paleo-age of sea floor, and paleo-geography of plate boundaries in a 3-D numerical model, we simulate the Farallon–Juan de Fuca subduction during the past 40 Ma. We find that the highly segmented upper mantle structure of western U.S. is a direct result of the Farallon subduction. We show that the tilted ‘horseshoe’-shaped fast seismic anomaly beneath Nevada and Utah at 300–600 km depth range is in fact a segment of curled slab subducted since 15 Ma, and the shallower linear slab beneath the Cascades is younger than 5 Ma. The distinct morphology between these two parts of the subduction system indicates the strong influence of the fast trench roll-back since 20 Ma, the northward migrating JF–PA–NA triple-junction, and the toroidal flow around slab edges. The observed mantle structures are used to constrain the rheology of the upper mantle through matching the shape, depth, and location of modeled subducted slab segments. The inferred viscosity for the asthenosphere is  $5 \times 10^{19}$  Pa s and those for the transition zone and lower mantle are  $1.5 \times 10^{21}$  Pa s and  $2 \times 10^{22}$  Pa s, respectively. The slab is found to be about 2 orders of magnitude stronger than the ambient mantle above 410 km depth, but of similar order of magnitude viscosity in the transition zone.

© 2011 Elsevier B.V. All rights reserved.

### 1. Introduction

The rich Late-Cenozoic geologic history and extensive ongoing tectonic activities over western United States are intimately tied to the Farallon–Juan de Fuca subduction and the mechanical interplay between the Pacific and North American plates (e.g., Atwater and Stock, 1998; Bird, 2002; Humphreys, 1995; McQuarrie and Wernicke, 2005). Recent deployment of the USArray seismic experiment has generated a vast amount of data, which, in turn, lead to a still growing pool of tomographic models (e.g., Burdick et al., 2008; Obrebski et al., 2010; Roth et al., 2008; Schmandt and Humphreys, 2010; Sigloch, 2011; Tian et al., 2011). Although still differing at fine scales ( $\sim 100$  km), these seismic inversions show a clear trend of consistency in outlining a similar pattern of 3D mantle structures beneath the western U.S., especially regarding the fast seismic anomalies (Fig. 1). These high-resolution images, therefore, become a powerful constraint for studying the corresponding mantle dynamics of western U.S. While earlier works based on mostly lower mantle Farallon images provide insights on the dynamic evolution of North America during the Late Cretaceous to early Tertiary (Bunge and Grand, 2000; Liu et al., 2008), a better understanding of the subsequent tectonic history will rely on an improved upper mantle seismic image, as revealed by recent tomography studies.

Interpretation of the observed mantle structures, however, is not always straightforward. Part of the reason is that these static images are the cumulative result of subduction over time, which is affected by many factors such as initial conditions, boundary conditions, and mantle and slab rheology (Billen and Hirth, 2007; Liu and Gurnis, 2008; Stegman et al., 2010a;). Another difficulty comes from the apparent 3-D morphology of these seismic structures, which does not fit with a simple 2-D subduction configuration. For instance, the fast ‘horseshoe’-shaped seismic anomaly below Nevada and Utah, as imaged by most tomography models (Fig. 1), has been interpreted as either a lithospheric drip due to gravitational instability (West et al., 2009), or a delaminated Laramide flat slab (Schmandt and Humphreys, 2010), or a slab fragmented by fracture zones (Sigloch, 2011) and/or a putative mantle plume (Obrebski et al., 2010). Measurements of seismic anisotropy, a proxy for internal deformations of Earth (Long and Becker, 2010), can provide more information about mantle dynamics. But the answer is still not unique. As an example, SKS splitting measurements display a circular pattern largely centered over Nevada, and has been attributed to either a toroidal mantle flow around the southern edge of the down going Juan de Fuca slab (Zandt and Humphreys, 2008) or a vertically sinking mantle drip beneath the Great Basin (West et al., 2009).

A further differentiation of these proposed mechanisms will require more data constraints, especially those involving the temporal evolution. Tectonic plate motions, originating from the internal convection of mantle (Lithgow-Bertelloni and Richards, 1998), are an apparent time-dependent observable. Movements of plates relative to

<sup>\*</sup> Corresponding author.

E-mail address: [lil019@ucsd.edu](mailto:lil019@ucsd.edu) (L. Liu).

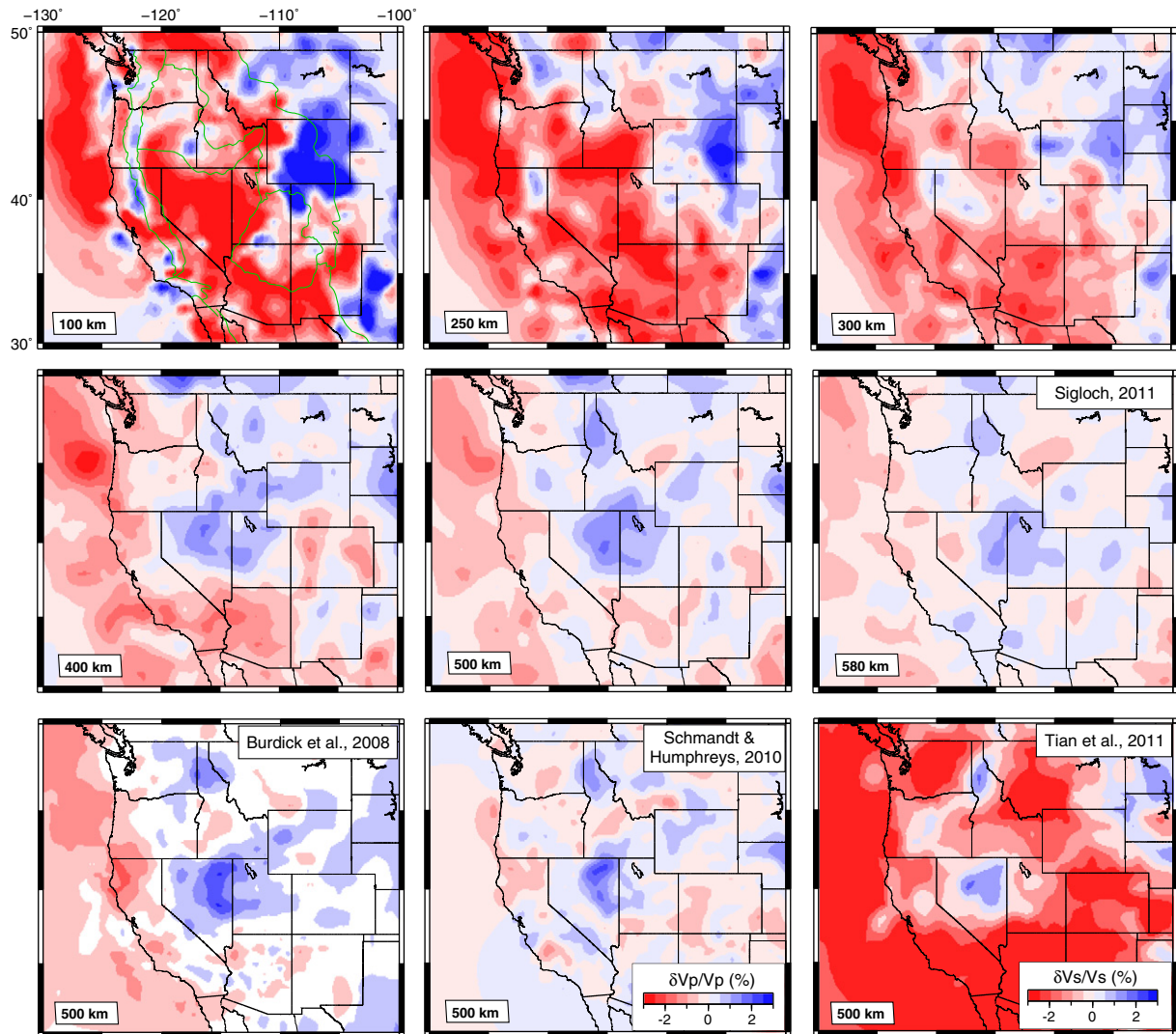


**Fig. 1.** Seismic structure of the western U.S. upper mantle, imaged by four recent tomography models derived with different methods and data sets: the upper and middle rows are from the P-wave model by Sigloch (2011); for comparison, two other P-wave models (Burdick et al., 2008; Schmandt and Humphreys, 2010) and one S-wave model (Tian et al., 2011) are shown at the bottom for the depth of 500 km. Note the agreement on the pattern of fast seismic anomalies among all these different tomography inversions.

the deep interior, when used in conjunction with other geological records such as surface vertical motions (Gurnis et al., 1998; Liu et al., 2008) or ancient tectonic events (Bunge and Grand, 2000), can help identify the nature of present-day mantle structures and their dynamic consequences to the surface. Plate motion induced mantle flow also helps to predict the record of seismic anisotropy (Becker et al., 2006; Jadamec and Billen, 2010). Internal deformation of a tectonic plate, such as the Basin & Range (B&R) extension over western U.S. (e.g., McQuarrie and Wernicke, 2005), may also reflect the underlying mantle processes such as a mantle plume impinging under the continent (Parsons et al., 1994), or subduction with a shrinking slab

width (Schellart et al., 2010), or simply due to the temporal variation of surrounding tectonic stresses (Choi and Gurnis, 2003).

In this paper, we present a model in which we attempt to simulate the Farallon–Juan de Fuca subduction since 40 Ma. The objective of this study is to reproduce the observed seismic structures associated with subduction below western U.S., while investigating the effects of mantle and slab rheology on subduction dynamics.

## 2. Model setup

In order to model subduction and associated mantle flow, we use the 3D spherical finite element code for mantle convection, CitcomS (Zhong et al., 2000). The code solves for an incompressible Newtonian fluid within a spherical mantle shell. Table 1 lists the basic model parameters we use in these models.

### 2.1. Mesh parameters

Our regional model adopts a mesh with  $257 \times 257 \times 65$  nodes in latitude  $\times$  longitude  $\times$  depth, covering a physical domain of  $60^\circ \times 100^\circ \times 2760$  km, respectively. The mesh is largely centered on western U.S., with variable grid spacing in all three dimensions such that the numerical resolution increases toward the center and the surface. The finest

**Table 1**  
Summary of model parameters.

Parameter	Value
Radius of the Earth	6371 km
Gravitational acceleration	$9.81 \text{ m s}^{-2}$
Reference mantle density	$3300 \text{ kg m}^{-3}$
Reference viscosity	$10^{21} \text{ Pa s}$
Thermal diffusivity	$10^{-6} \text{ m}^2 \text{ s}^{-1}$
Density change across the 410 km phase transformation	$-660 \text{ kg m}^{-3}$
Density change across the 660 km phase transformation	$330 \text{ kg m}^{-3}$
Temperature change across the lithosphere	$400^\circ \text{C}$

mesh grid with a block size of  $12 \times 20 \times 7$  km occurs in the uppermost mantle beneath western U.S. To avoid artificial return flow from side walls, we have chosen a wide enough box, with the nearest vertical boundary being  $>2000$  km away from any part of the western U.S. Furthermore, we add a vertical weak zone all around the box to accommodate possible return flows, a technique also employed by [Jadamec and Billen \(2010\)](#).

In order to obtain a good radial resolution while sampling a large enough depth of the mantle, we vary the vertical resolution for depth of  $>200$  km such that the total 65 nodes span depths of 1000, 2000 and 2891 km, respectively. We find that these three meshes produce very similar slab structures above 500 km, but the one with 1000 km depth leads to a limited slab penetration into the lower mantle, due to the small thickness of this mantle layer. Models presented here use a mantle depth of 2000 km or more.

## 2.2. Boundary conditions

On the top surface, the model takes the plate reconstruction by [Müller et al. \(2008\)](#) as the velocity boundary condition (Fig. 2A, B). All other boundaries are slip free. We also incorporate the temporally evolving plate boundaries into our model in order to track the position of the subduction zone (Fig. 2A), as well as to test the dynamic effect of the rheology structure of these boundaries. All the time-dependent paleo information including plate motions, plate boundary coordinates, and seafloor ages are interpolated down to a 1-million-year interval via the open source paleo-geographic software GPlates ([Gurnis et al., submitted for publication; www.gplates.org/](#)). In order to account for the differential motion of the Farallon trench relative to the stable North

America during the B&R extension, we calculate the trench velocity from the paleo-longitude of subduction zones and interpolate its difference from that of stable North America within a narrow zone ( $\sim 300$  km) behind the trench.

The model assimilates paleo seafloor ages from the same reconstruction to prescribe a top thermal boundary layer with a constant surface temperature of 300 K. Under the continent, a zero heat-flux boundary condition is applied (Fig. 2A, B), similar to the technique adopted by earlier workers ([Christensen, 1996; Tan et al., 2002](#)). Artificial (or numerical) diffusion is a common problem for numerical models in that a finite grid resolution tends to smear sharp thermal gradients, such as that within a temperature boundary layer ([Davies et al., 2007](#)). Although the adaptive mesh refinement technique is a solution ([Davies et al., 2007; Stadler et al., 2010](#)), its implementation in a 3D code solving for the time evolution of mantle flow is not a trivial task. Here we approximate the thermal structure of the oceanic plate through a modified error function that uses a reduced temperature gradient ( $\sim 400$  °C instead of  $\sim 1000$  °C temperature change across the lithosphere) but maintains an equivalent negative buoyancy as the larger temperature drop when integrated over the thickness of the lithosphere (Fig. 2C). For the mesh employed in these models, this approximation improves the resolution of the thermal boundary layer without hampering the subduction dynamics. One advantage of this ‘smeared’ representation of the thermal lithosphere is that the resulting slabs at depth have an apparent thickness similar to that of the seismically imaged slabs, which are also a ‘filtered’ version of real structures ([Ritsema et al., 2007](#)).

A free surface function is preferred for modeling subduction evolution, especially for obtaining the realistic slab geometry in the vicinity

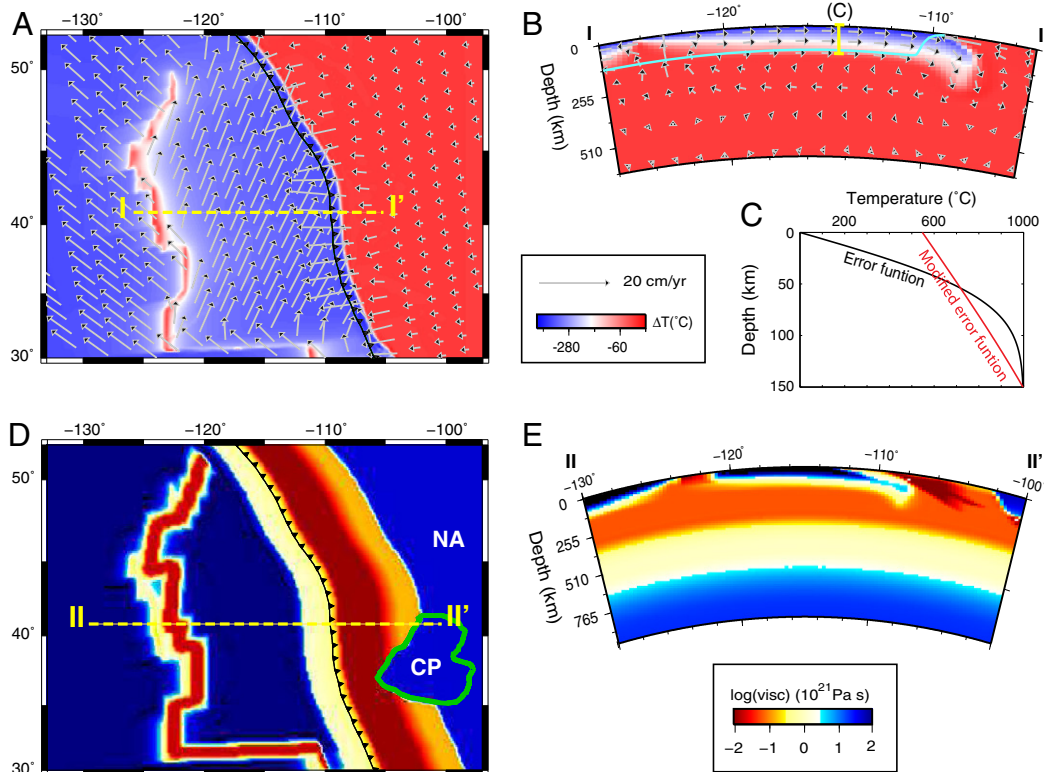


**Fig. 2.** A snapshot at 35 Ma illustrating the boundary conditions and viscosity structures used in the forward model. (A) Velocity and temperature fields at 23 km depth. The dashed profile line is for panel B. (B) Vertical cross-section of the upper mantle showing a subducting slab developed from the assimilated thermal boundary layer. The solid cyan curve marks the lower bound of temperature assimilation. (C) The modified error function thermal profile adopted in this study across the upper 150 km (the vertical yellow bar in panel B), in order to overcome numerical diffusion due to limited mesh resolution within the lithosphere and subducting slabs. For reference, a standard error function profile is also shown. (D) Laterally varying viscosity structure at 23 km depth including rigid oceanic and continental plates and plateaus, weak plate boundaries, moderate slab hinges, and a weak mantle wedge. NA is for North America; CP for Colorado Plateau (within the green contour). (E) A vertical viscosity profile along the dashed line in panel D illustrating the depth range of the four layers: lithosphere, asthenosphere, transition zone and lower mantle. Lateral viscosity variations due to temperature dependence and plate boundary features are also shown.



of a subduction zone as found in laboratory experiments (Schmeling et al., 2008). Schmeling et al. (2008) proposed a 'sticky air' layer above a pure viscous model to simulate subduction, with the essence of this layer being low-viscosity and zero-density. This 'sticky air' function, however, requires a very high numerical resolution at shallow depth, and a more serious problem with this technique for our model is that it is likely to decouple the imposed surface velocities from the interior due to the weakness of this layer. We reformulate this 'sticky air' function into a phase transformation within the uppermost 2 elements of the model (~15 km) such that cold material within this layer gains some extra negative buoyancy, in order to mimic the lateral pressure gradient at a convergent boundary due to the low topography of trench. This will cause the slab to sink more easily but only at places with a low enough viscosity such as subduction zones. This effectively mimics the zero-density 'sticky air' implementation since they both increase the lateral gradient of buoyancy that promotes the plate's tendency to sink asymmetrically at the subduction front. Tests indicate that the existence of the 'sticky air' layer helps the generation of a smooth slab (no material stuck on the overriding plate), as well as producing a smaller slab dip angle due to the extra dynamic pressure originated from the trench-side sea-floor topography (Supplementary Fig. S1).

### 2.3. Rheology

We use both depth and temperature dependent viscosity in this calculation (Fig. 2D, E). A maximum of 4 layers of viscosity structure is assumed, including lithosphere, asthenosphere, transition zone, and lower mantle. The asthenosphere here extends from the base of the lithosphere to ~300 km. The radial viscosity profile is smoothed between adjacent layers over a vertical distance of 50 km between the lithosphere–asthenosphere and over 100 km for deeper interfaces (Fig. 2E). Density changes due to the phase transformation across the 410 and 660 km interfaces were also varied in some models, but models shown here use fixed values from Table 1.

Lateral variation of viscosity is achieved firstly from its temperature dependence, assuming a Newtonian fluid (Fig. 2E and Supplementary Fig. S2). This can lead to an increase of slab viscosity by up to 4 orders of magnitude relative to the ambient mantle. Although it is generally accepted that the upper mantle is non-Newtonian, our knowledge on the rheological strength of subducting slabs and deforming mantle is still not perfect (Billen and Hirth, 2007; Stegman et al., 2010b; Stadler et al., 2010). We circumvent this problem by applying a cap value to the strong temperature dependence of the slab, such that the effective viscosity of slabs can be evaluated by comparing predicted and observed slab morphology at present day. The test on relative strength of the slab in this exercise is motivated by other studies of effective viscosity in which modeled slabs exhibit recumbent folding behavior in response to encountering a more viscous lower mantle (Schellart et al., 2007; Stegman et al., 2010b). Slabs in this folding regime are distinct in their ability to develop lateral trench curvature in response to slabs curling from the surrounding toroidal mantle flow (Funicello et al., 2004; Morra et al., 2006; Royden and Husson, 2006; Schellart, 2004; Schellart et al., 2007; Stegman et al., 2006). Additionally, the along-trench width of such slabs controls a transition from subduction being accommodated through forward plate advance to being accommodated more by trench retreat and slab rollback (Schellart et al., 2010).

Besides the temperature-dependent rheology, the fine resolution mesh as used here allows for implementation of many realistic structural features with even more dramatic viscosity gradients. In total, over 200 model runs were performed in which many specific aspects were investigated including narrow plate boundaries (being vertical at mid-ocean ridges and transform faults, and one-side dipping above down going slabs), slab hinges (weak bending part of the slab with a stronger core), a mantle wedge (a weak zone between the surface and the slab), and large rheological variations from the B&R province to the

Colorado Plateau (CP) and the cratonic North America (NA) (Fig. 2D, E). The model can effectively achieve a viscosity contrast up to 4 orders of magnitude within a ~100 km distance (Fig. 2D, E). The resulting strong 3-D viscosity variation is essential for the generation of asymmetric subduction and a physically reasonable subducting slab (Figs. 2B and 3A). Tests with a progressive amount of plate boundary features indicate that the existence of a weak subduction zone (including the mantle wedge) is critical for the generation of an efficient and localized return flow above the slab causing a trench rollback at the observed rate (Fig. 3A and Supplementary Fig. S2).

## 3. Results and discussions

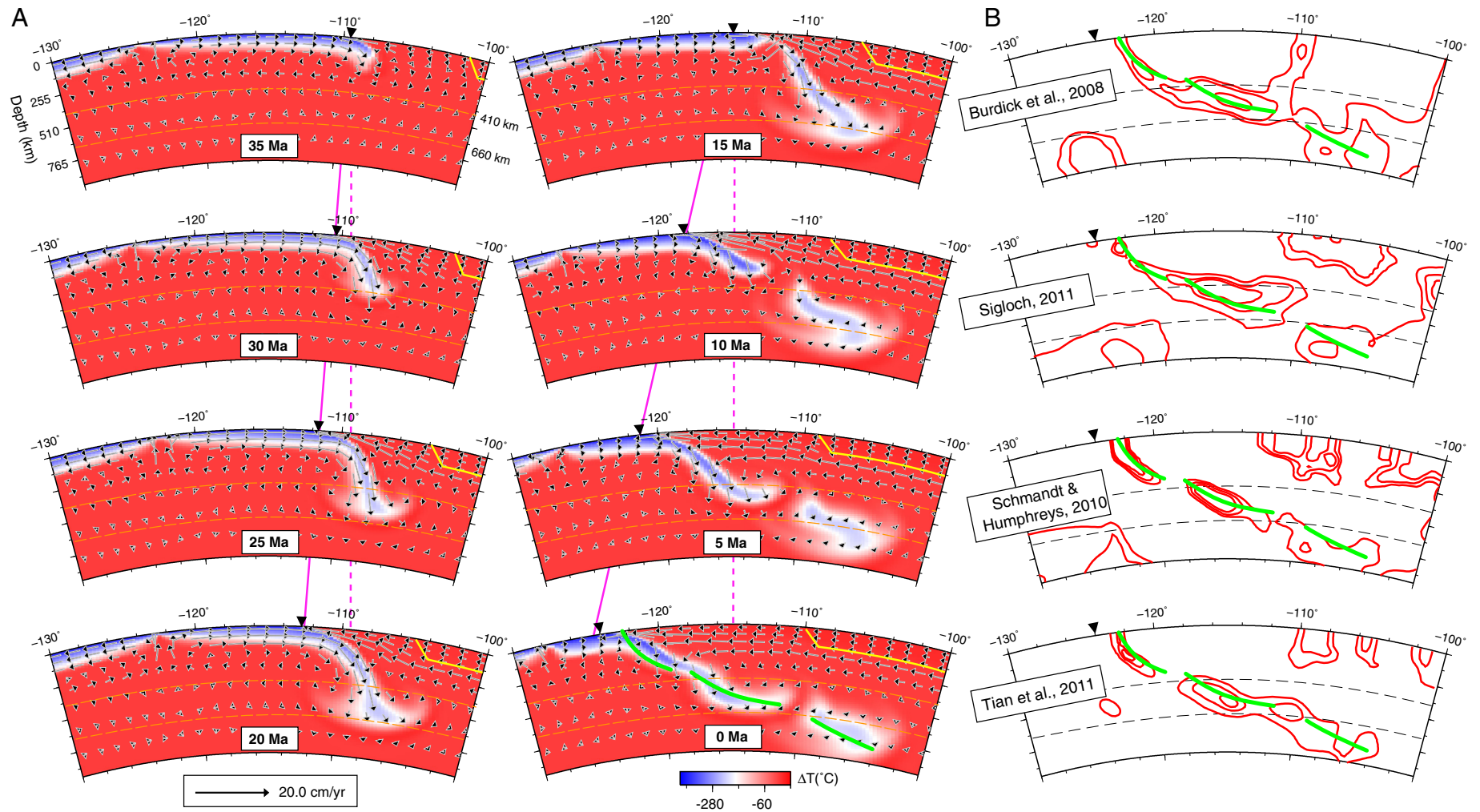
In this section, we present a model that best predicts the major tomographic features (fast anomalies only) beneath western U.S., which also provides a good constraint on the viscosity of the upper mantle and slabs.

### 3.1. Late Cenozoic Farallon subduction

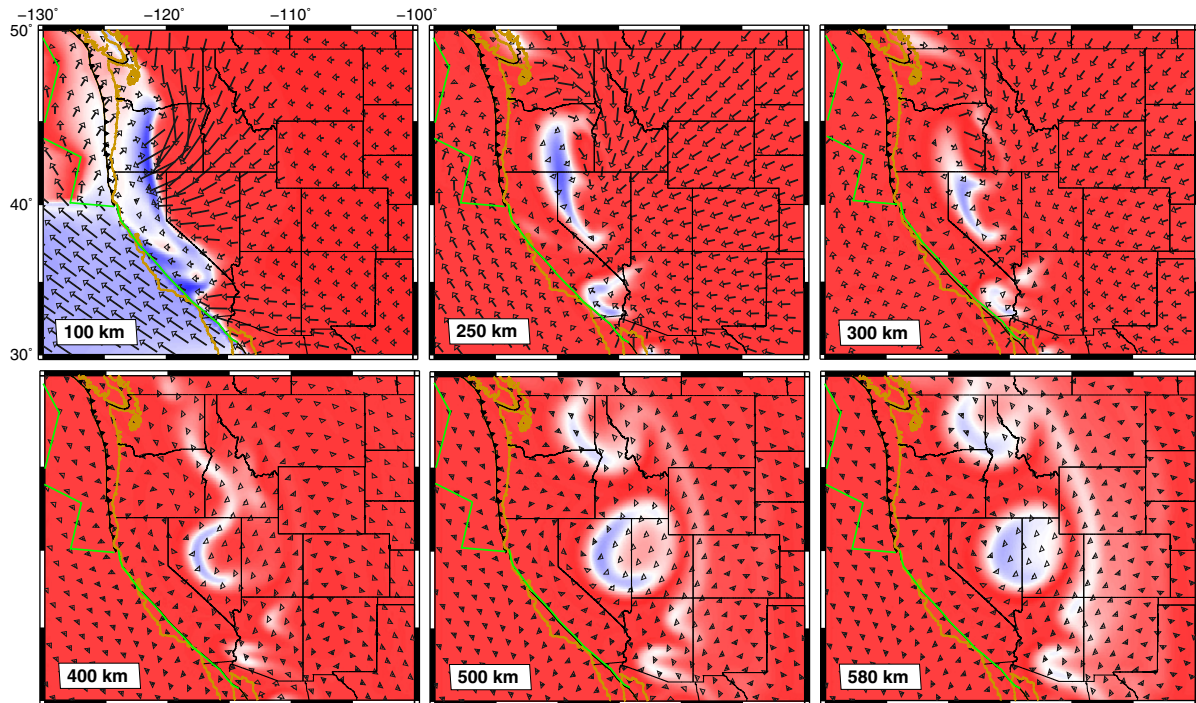
It is now well accepted that the flat-slab subduction of the Farallon plate during the Late Cretaceous to early Tertiary greatly affected the geology of western U.S. (Bird, 1988; DeCelles, 2004; Humphreys, 2009; Liu et al., 2010). This flat subduction largely came to an end during the Late Eocene to Oligocene, as evidenced by re-establishment of the trench parallel magmatic arc (e.g., Humphreys, 1995). To model the post-Laramide Farallon subduction, our simulation starts at ~40 Ma and integrates to the present day. In fact, models with the initial age varying from 30 Ma to 40 Ma have little difference in the predicted present day upper mantle structure. Furthermore, the observation that many seismic tomography models reveal a quasi-linear N–S slab gap at depths of ~800 km beneath central US supports the establishment a new subduction regime of the Farallon plate during the Late Eocene (e.g., Schmandt and Humphreys, 2010; Sigloch, 2011; Sigloch et al., 2008).

Fig. 3 illustrates the modeled Farallon plate subduction since 35 Ma along latitude 41°N. The evolution of subduction demonstrates a clear dichotomy for times before and after 20 Ma, which marks the commencement of the B&R extension at this latitude. Subduction prior to 20 Ma is characterized by fast down-going plate (5–10 cm/yr in the E–W projection) with a slow rate of trench retreat (~2 cm/yr). This speed of trench motion is similar to the westward motion of the stable North America (yellow outline in Fig. 3), suggesting little internal deformation within the overriding continent. The Farallon slab has a normal dipping angle at ~60° up to 25 Ma, with a localized return flow occurring inside the mantle wedge above the slab. Since 20 Ma, the start of the B&R extension also leads to a much faster trench retreat of up to ~6 cm/yr, pushing the subduction zone away from the continental interior. The subduction process during this time period switches to a slab rollback dominated mode, with the eastward Farallon plate velocity greatly reduced (down to ~2 cm/yr). This transition of subduction style is controlled by the continuously shrinking width of the subducting slab (Schellart et al., 2010). Consequently, this results in a shallower-dipping (~30°) Farallon slab for most of the time. A fast returning wedge flow of up to 20 cm/yr exists in a broad region above the slab, accommodating the differential motions between the back-lying slab and the overriding plate.

Besides the different dip angles, the transition in the style of subduction at ~20 Ma also causes a change in slab morphology (Fig. 3). Specifically, the fast subduction before 20 Ma leads to steeply dipping linear slabs with simple down-dip geometry. The slow-down of the Farallon plate velocity after 15 Ma, together with an enhanced trench rollback, leads to more shallowly dipping slabs in the mantle, whose geometry is more prone to be affected by the viscous layering (depth-dependence) of the mantle than a vertical slab, as seen from the depth variation of the slab curvature. Particularly at present day, the geometry of the



**Fig. 3.** Temporal evolution of Farallon subduction since 35 Ma along the present-day latitude 41°N. (A) Prediction from the best-fit model. The black inverse triangle represents trench locations. Solid yellow lines mark the bottom of the strong continental lithosphere. Solid magenta lines track the westward trench migration through time, with the dashed magenta line as a fixed reference. The thick green lines at 0 Ma represent the seismically observed slabs. (B) Contours of present-day slab structure imaged by four different tomography models. Each model is represented by three levels of contours indicating the gradient of seismic anomalies.



**Fig. 4.** The predicted present-day mantle temperature fields at five depths same as those chosen for the tomography images in Fig. 1. Brown lines represent coastlines, and green lines mid-ocean ridges and transform plate boundaries. Both the color and velocity scales are the same as those in Fig. 3.

Farallon slab along this latitude resembles the ‘double-slab’ (thick green lines in Fig. 3) reported by several research groups (e.g., Burdick et al., 2008; Schmandt and Humphreys, 2010; Sigloch, 2011; Tian et al., 2011), validating our model prediction.

### 3.2. Segmentation of the Farallon slab

In order to better envisage the modeled mantle structure at present day, we provide a sequence of maps of the temperature field (Fig. 4) at the same depths as those chosen for the tomography image shown in Fig. 1. A comparison between Figs. 1 and 4 suggests that the predicted slab morphology matches the majority of fast seismic anomalies excluding features related to the continental North America. These include the continuous linear slab under Cascadia at shallow depth (100 km), the break down of the linear pattern at ~300 km in Nevada and Oregon, and the tilted ‘horseshoe’ at larger depths beneath Nevada and Utah (>300 km). The model also seems to predict some other fine-scale features such as the transition zone fast anomalies beneath northern Idaho and eastern Washington, and some shallow structures in southern California as well (Figs. 1 and 4). Here we will focus on the depth variation of slab morphology.

The good agreement achieved between the observed and predicted mantle structures suggests that the Farallon slab is highly segmented at depths, whose upward connection with the shallower Cascadia slab forms a complex slab network at ~300 km around the corner of Oregon, Idaho and California. The westward rollback of the linear slab near the surface and vertical sinking of the 3-D slab complex at depth leads to a strong clockwise toroidal flow around slab edges within the low-viscosity asthenosphere under Washington, Oregon and Nevada (Fig. 4). Furthermore, the pattern of the toroidal flow varies rapidly with depth such that it takes a spiral shape with the flow direction rotating by more than 90° within a narrow depth range of ~200 km, i.e., the flow under Washington switches from being eastward at 300 km to southward at 100 km, and that under Oregon from southeastward to southwestward. This pattern of edge-driven flow is similar to that proposed by Zandt and Humphreys (2008),

although with a more complicated configuration. This difference is, of course, not surprising given the more sophisticated slab geometry developed in this study.

In order to understand the process of slab segmentation, we backtrack the evolution of the subducting Farallon slab. Fig. 5 illustrates the 3-D slab geometry at several different time snapshots since Late Early Miocene. At 20 Ma, the slab still behaved as a continuous linear sheet along the entire subduction front. Due to the commencement of the B&R extension around this time associated with a narrowing surface oceanic plate, the shallow part of the slab started to flatten. This can be seen from the steeper slabs to the south of the triple junction (Fig. 5) and those at earlier times (Fig. 3A), both associated with older subduction. Up to 15 Ma, accompanying the deceleration of the eastward motion of the Farallon plate and the accelerating westward trench retreat, the down going slab was torn apart by the still fast sinking slab at depth and the excess sub-slab dynamic pressure (Fig. 3A). A slab gap had developed by this time at the depth of 20–100 km, where the younger slab to the west of the gap formed a tongue-shaped flat-slab, and the older part to the east was still steeply dipping (Fig. 5). The slab to the north of 46°N and south of the triple junction was still intact. By 12 Ma, the slab tear sank to 200–300 km depth, where the gap was much broadened in the east–west direction. Due to gravitational instability, the tongue-shaped flat Farallon slab eventually collapsed, buckling downward from its eastern edge, and started to form a separate slab.

The fact that this slab tear initiated in the middle part of the subducting plate (~44°N) rather than along the entire trench suggests that this event was not entirely due to the differential motion along the down-dip direction, but is subject to the greater dynamic pressure below the center compared to the edge of the slab. This dynamic pressure gradient is best illustrated by the outward toroidal flow from beneath around slab edges in simple 3D models (e.g., Stegman et al., 2006), as well as the overall concaved trench geometry and smaller slab dip at the central part (e.g., Fig. 5). If we reduce this dynamic pressure by removing the ‘sticky-air’ layer from the top of the oceanic plate, the slab tear won’t happen around this time and the present-day



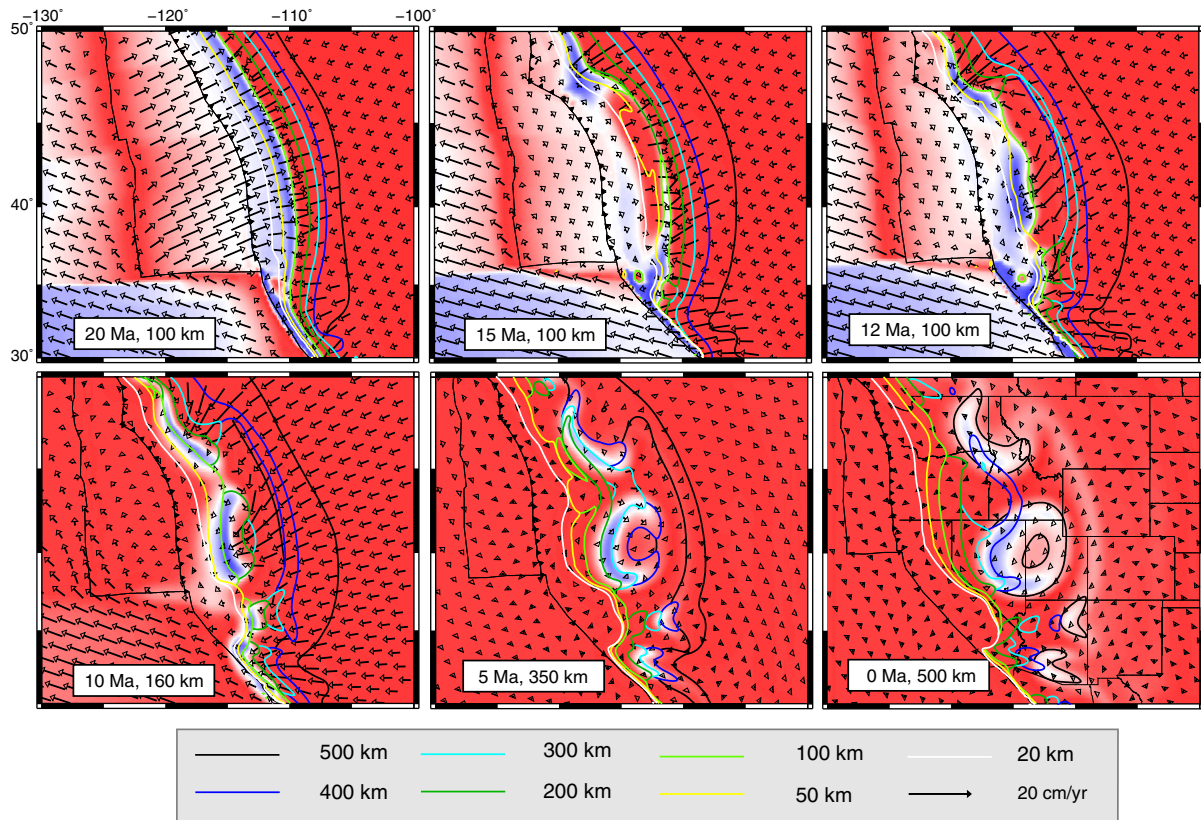


**Fig. 5.** A pseudo 3D visualization of the evolving Farallon slab system since 20 Ma. The bold color lines represent the upper boundaries of slab at different depths, with a darker color for a larger depth, assuming a view perspective from the top. For a given snapshot, both the background temperature and the velocity field are shown for the specified depth. Color scale same as Fig. 3.

mantle structure is not predicted either (Supplementary Fig. S1). More tests with different mantle viscosity profiles indicate that, without the 'sticky-air', the model can never reproduce the transition zone 'horseshoe' fast anomaly as observed in seismic tomography (Fig. 1), which requires the Farallon slab to break at ~15 Ma.

With rollback being the dominant mode of subduction after 15 Ma, strong returning flows occurred everywhere along the mantle wedge. The pattern of return-flow, however, was not invariant along the subduction zone (e.g., Fig. 5), as was interrupted by the gaps inside the slab. For a subducting slab with a finite width of less than 1500 km, the toroidal return-flow tends to focus toward the central part of the mantle wedge (Schellart et al., 2007; Stegman et al., 2006), and our model confirms this observation (Figs. 4 and 5). Following the first break-up at 15 Ma, the subsequent Farallon slab evolved into three separate segments, but the southernmost piece consisted of highly fragmented abandoned slabs left behind by the N–S shrinking surface plate. The three slab segments evolved almost independently since their breaking off, with the strongest return-flow occurring right above the slab surface (e.g. at 10 Ma). The return flow is also segmented as localized corner-flows are intervened by toroidal flows around slab edges, where the flow direction rotates by up to 180° from the center of the gap to above the slab (Figs. 4 and 5). Effectively, the differential flow across the slab surface caused the slab to fold upwards and outwards at edges, forming a progressively curved geometry toward the present day.

Since the subducting slab at shallow depth is a coherent sheet continuous from the surface thermal boundary, its down-dip connection with the already segmented slabs leads to a complex transitional geometry at mid-upper mantle depth. The temporal evolution of the Farallon subduction further reveals that this complex slab configuration had largely existed during the past 15 Ma, although with an increasing level of complexity toward the present day. A closer look at Fig. 5 suggests that the Farallon slab is segmented not only in the trench-parallel but

also the down-dip direction, as a result of the competition between the speeds of slab folding and trench rollback. For instance, some down-dip tears formed isolated slab 'pockets' within 100–400 km depths at the northern and middle part of the subduction system during the past 5 Ma (Fig. 5). However, we have to point out that the details of these slab tears are sensitive to the rheology structure of the mantle and slabs, as will be discussed more in the next section. The exact rheology and thus shape of these secondary slab tears are not definitively constrained, given the uncertainties in both the tomography images and plate reconstructions used in this study.

### 3.3. Implication for mantle and slab viscosities

Although all recent tomography images based on the USArray data acknowledge a highly 3-D mantle structure below western U.S., the most consistent features are limited to the trench-parallel linear Juan de Fuca slab above 200 km and an eastward dipping cylinder-shaped fast anomaly below 300 km beneath Nevada and western Utah, together with a slab gap below south Idaho within the transition zone (e.g., Burdick et al., 2008; Schmandt and Humphreys, 2010; Sigloch, 2011). Slightly less well agreed upon are the fast seismic anomalies beneath Washington, Oregon and Idaho (Fig. 1), part of these was referred to as a 'slab curtain' by Schmandt and Humphreys (2010). Prediction of these seismic features provides a constraint for the viscosity structure of the mantle and slabs (Figs. 6 and 7).

The sinking depth of a slab inside the mantle during a given time period is a measure of mantle viscosity, given the absolute viscosity of the slab and its density profile defined by paleo sea floor ages (Figs. 2A and 3A). Tests show that the upper mantle layer with the smallest viscosity affects slab speed and thus penetration depth the most, provided the existence of a weak enough subduction zone decoupling the slab from the overriding plate. By assuming that the asthenosphere is weaker

than all other layers, we look for an appropriate viscosity that best predicts the observed slab geometry. Slabs sinking through an asthenosphere with a viscosity ( $\eta_{\text{asth}}$ ) as low as  $10^{20}$  Pa s cannot reach the depth as observed, while that through a much weaker asthenosphere ( $10^{19}$  Pa s) seems to have sunk too deep by now; an intermediate viscosity ( $5 \times 10^{19}$  Pa s) gives rise to the best prediction (Fig. 6A). This constraint can also be seen from the pattern of lateral structures, where a weaker (stronger) asthenosphere drops slabs closer to (further from) the trench, given the rate of trench rollback (Fig. 7A).

Slab morphology, on the other hand, provides a measure for the strength of the slab (e.g., Billen and Hirth, 2007; Stegman et al., 2010b). For the given plate kinematics imposed at the surface, a strong slab is more resistant to bending and to deformation at depth, resulting in a shallower subduction with limited slab penetration, while a very weak slab tends to subduct more easily and to break at shallow depth, forming slab piles in the transition zone (Ribe et al., 2007). This is shown in Fig. 6B where distinct results come from a small variation of slab viscosity ( $\eta_{\text{slab}}$  differs by a factor of 10). In a map view, a large viscosity results in thick and stagnant slabs sitting at shallow depth, while a weak slab forms tenuous structures in the asthenosphere and dumps most slab material into the transition zone (Fig. 7B). Overall, these results favor a slab with a viscosity of  $5 \times 10^{21}$  Pa s, which is about two orders of magnitude stronger than the ambient asthenosphere. However,

given the ‘smeared’ representation of slabs with a suppressed thermal gradient (Fig. 2B), we expect the actual viscosity contrast between the strongest slab core and the ambient asthenosphere to be larger. Indeed, this study constrains the average effective viscosity of the whole slab, rather than the detailed viscosity profile across the slab. The effective mechanical strength is the more relevant property in modulating slab evolution than the details of how the strength is distributed in any particular viscosity profile (Ozbench et al., 2008).

It is clear from these experiments that the slab has to be significantly stronger ( $>100$ ) than the ambient upper mantle. However, how much stronger the slab could be relative to the mantle seems elusive, given a plausible competition between a strong slab and a weak mantle on affecting the sinking speed of slabs. This is a reasonable concern for a continuous slab whose connection with the surface plate forms a stress guide along the slab. This is, however, not true if the slab is mechanically decoupled from the actively subducting plate, such as the southernmost Farallon segment (Fig. 5). In this case, the sinking speed of these isolated slabs mostly depends on the ambient mantle viscosity. For an example, in Figs. 6A and 7A, the case with the weakest asthenosphere produces slab structures similar to the best-fit model at latitudes where active subduction zone exists, but the predicted southernmost slab branch is too prominent to be real (Fig. 7A), since none of the tomography models image this structure.

A similar exercise can apply to constraining the viscosities of the transition zone and its slabs. As Fig. 6C illustrates, transition zone viscosity is inversely related to the depth of slab penetration. This relationship is cleaner than that for the asthenosphere viscosity (Fig. 6B), whose variations also likely affect the dynamics of the subduction zone, another influential factor but which we try to keep fixed for all tests. Variation of transition zone viscosity also clearly affects the lateral slab patterns (Fig. 7C), where a larger viscosity leads to a more linear slab with little bending, and a smaller viscosity causes highly fractured slabs. Together with Fig. 5, these experiments indicate that the transition zone rheology strongly affects the folding of the segmented slabs at depth. In the transition zone, effects of slab viscosity relative to the mantle is not as prominent as that in the asthenosphere, but our preferred model favors a transition zone slab weaker than its asthenosphere counterpart, i.e., no stronger than  $5 \times 10^{21}$  Pa s, because, otherwise, the ‘double-slab’ feature (Figs. 4 and 6), which requires a viscosity reduction inside the slab across 410 km, could not be predicted. In fact, among all tests performed, only the best-fit model predicts this rather subtle feature.

The constraining power on the lower mantle viscosity is more limited, due to both the smaller portion of slabs within this layer and the increasing uncertainty in seismic images (Fig. 3). We do find that in order for the deepest segment of the slab to reach  $\sim 800$  km (e.g., Fig. 3), as indicated by most tomography models, the lower mantle viscosity should be no larger than  $2 \times 10^{22}$  Pa s. Therefore, the model that best predicts tomography has a viscosity layering (without temperature-dependence) of 100, 0.05, 1.5, and  $20 (\times 10^{21}$  Pa s) for lithosphere, asthenosphere, transition zone, and lower mantle, respectively. The strong lithosphere is largely an a priori assumption, which may in fact represent a lower limit of its strength. This inferred viscosity profile is similar to inferences from our earlier work by predicting dynamic topography using an inverse convection model (Liu et al., 2008; Spasojevic et al., 2009), but this study has a more specific constraint on the viscous layering above 660 km.

The magnitude of lateral viscosity variation is another new outcome from this study compared to our earlier work. Besides the inferred slab viscosity, we could also place some constraints on the rheology of the mantle wedge and overriding plate. In order for the deforming slab hinge to follow the trench consistently with time, a fast enough corner flow must exist above the slab at shallow depth (e.g., Fig. 3). This in turn requires a weak enough mantle wedge, with a viscosity as small as  $10^{19}$  Pa s (Fig. 2D, E). The lateral extent of the wedge is less well known, but presumably no wider than the slow seismic regions over western U.S. (Fig. 1). We also find that the thickness of the strong

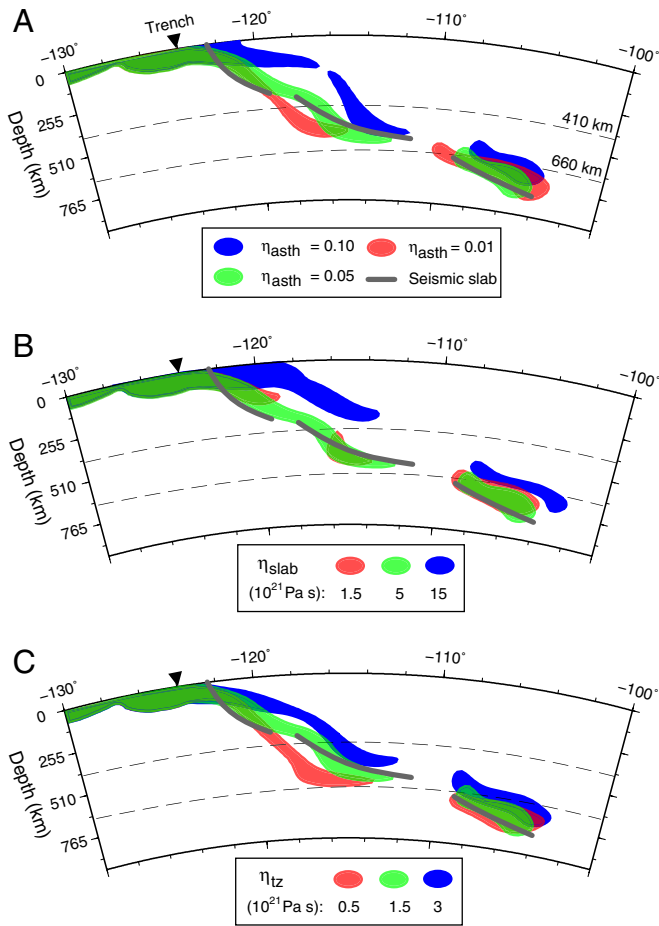


**Fig. 6.** Constraining mantle and slab viscosity (cross sectional view along latitude  $41^\circ\text{N}$ ). Variations in slab morphology due to changes in (A) asthenosphere viscosity (values relative to  $10^{21}$  Pa s), (B) asthenosphere slab viscosity, and (C) transition zone viscosity, respectively, while holding all other viscosities fixed. The colored areas represent the slab interior  $>150^\circ\text{C}$  colder than the ambient mantle, while different colors indicate different tests. The three pieces of thick grey lines represent the geometry of the seismically imaged slabs at this latitude (same as in Fig. 3).



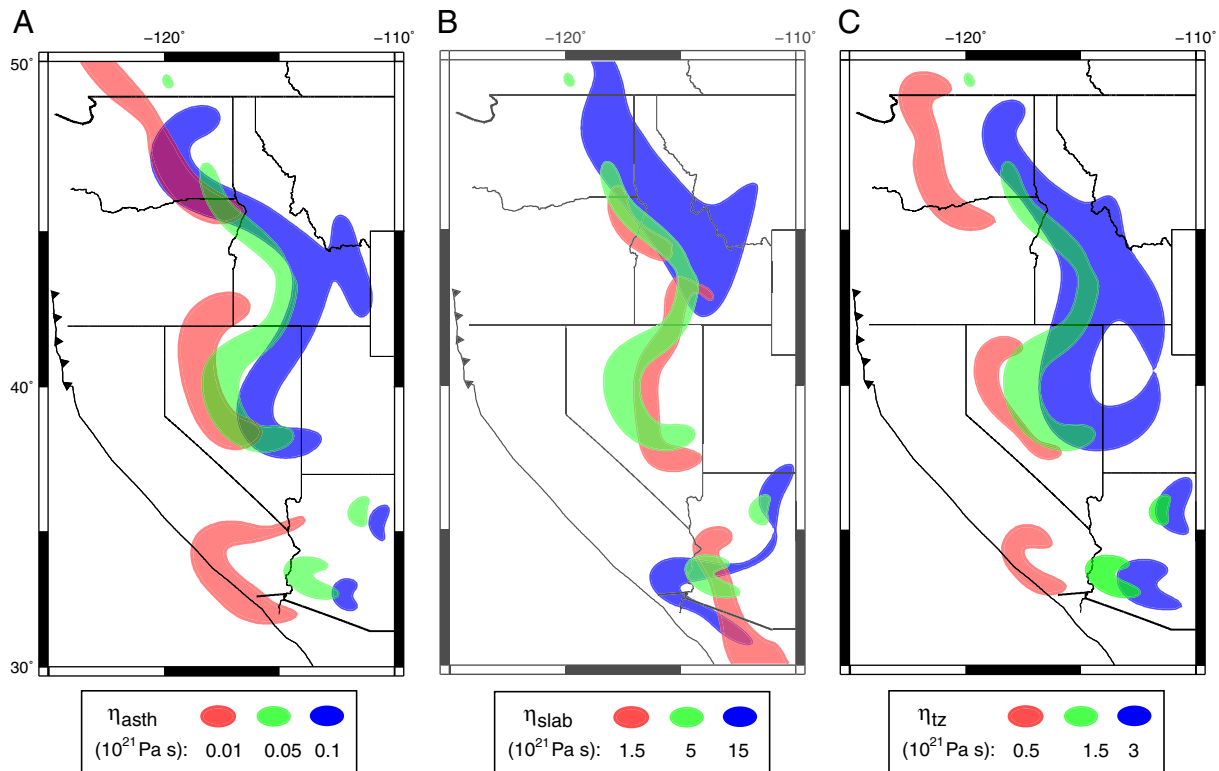


Fig. 7. Constraining mantle and slab viscosity (map view at 400 km depth), otherwise same as Fig. 6.

craton/CP has little effect on the evolution of slabs, as long as the mantle wedge is weak enough to decouple the slab from the overriding plate.

#### 4. Conclusion

In summary, we model the Late Cenozoic Farallon subduction by assimilating several types of observations including paleo sea floor ages, plate kinematics and plate boundary geometries. The model successfully reproduces the major seismic features associated with subduction. We find that the highly segmented upper mantle slab remnants are due to an initial slab break-up at ~15 Ma accompanying the slow-down of the Farallon plate and accumulated sub-slab dynamic pressure, followed by strong toroidal flows around edges of the segmented sinking slabs.

The present-day 'horseshoe'-shaped fast seismic anomaly below Nevada and Utah represents a highly folded slab subducted since 15 Ma. The upward connection of the deeper 3-D slab remnants with the surface plate leads to complex slab structures above the transition zone, which also generates a toroidal mantle flow whose magnitude and orientation vary rapidly with depth. Prediction of the observed seismic image also helps to constrain the rheology of the mantle and slabs above 800 km depth. Both the low viscosity upper mantle and weak slabs inferred from this study are consistent with the active surface tectonic history and young ages of the subducting plate.

Constrained by both well-observed boundary conditions, as well as the present-day seismic image, our geodynamic models have implications on several aspects of the geologic and tectonic history of the western US. Future work may include a quantitative understanding of the driving mechanisms for the lithosphere and crust deformation during the Late Cenozoic, the complex magmatic history of the Yellowstone hotspot system, and the peculiar seismic anisotropy measurements at the present day.

#### Acknowledgement

We are grateful to Brandon Schmandt and Yue Tian for sharing their tomographic models before being publicly made available, and to Allen McNamara and Claudio Faccenna for their helpful comments on improving the manuscript. A special thanks goes to Donna Blackman for several interesting discussions. Computational resources were provided by Teragrid project EAR100021. L.L. is under John Miles Fellowship and the Cecil and Ida Green Foundation. D.R.S. was supported in part by the G. Unger Vetlesen Foundation.

#### Appendix A. Supplementary data

Supplementary data to this article can be found online at [doi:10.1016/j.epsl.2011.09.027](https://doi.org/10.1016/j.epsl.2011.09.027).

#### Reference

- Atwater, T., Stock, J., 1998. Pacific–North America Plate tectonics of the Neogene Southwestern United States; an update, in: Ernst, W. G., and Nelson, C. A., eds., *Integrated Earth and environmental evolution of the Southwestern United States*; the Clarence A. Hall, Jr. volume: Columbia, Bellwether Publishing, p. 393–420.
- Becker, T.W., Schulte-Pelkum, V., Blackman, D.K., Kellogg, J.B., O'Connell, R.J., 2006. Mantle flow under the western United States from shear wave splitting, *Earth Planet. Sci. Lett.* 247, 235–251.
- Billen, M.I., Hirth, G., 2007. Rheologic controls on slab dynamics. *Geochim. Geophys. Geosys.* 8, Q08012. doi:10.1029/2007GC001597.
- Bird, P., 2002. Stress direction history of the western United States and Mexico since 85 Ma. *Tectonics* 21. doi:10.1029/2001TC001319.
- Bird, P., 1988. Formation of the Rocky Mountains, western United States: a continuum computer model. *Science* 239, 1501–1507.
- Bunge, H.-P., Grand, S.P., 2000. Mesozoic plate-motion history below the northeast Pacific Ocean from seismic images of the subducted Farallon slab. *Nature* 405, 337–340.
- Burdick, S., van der Hilst, R., Vernon, F., Martynov, V., Cox, T., Eakins, J., Mulder, T., Astiz, L., Pavlis, G., 2008. Model update December 2008: upper mantle heterogeneity beneath North America from P-wave travel time tomography with global and USArray transportable array data. *Seism. Res. Lett.* 80. doi:10.1785/gssrl.80.4.638.

- Choi, E., Gurnis, M., 2003. Deformation in transcurrent and extensional environments with widely spaced weak zones. *Geophys. Res. Lett.* 30. doi:[10.1029/2002GL016129](https://doi.org/10.1029/2002GL016129).
- Christensen, U., 1996. The influence of trench migration on slab penetration into the lower mantle. *Earth Planet. Sci. Lett.* 140, 27–39.
- Davies, D.R., Davies, H., Hassan, O., Morgan, K., Nithiarasu, P., 2007. Investigations into the applicability of adaptive finite element methods to two-dimensional infinite Prandtl number thermal and thermochemical convection. *Geochem. Geophys. Geosyst.* 8, Q05010. doi:[10.1029/2006GC001470](https://doi.org/10.1029/2006GC001470).
- DeCelles, P.G., 2004. Late Jurassic to Eocene evolution of the Cordilleran thrust belt and foreland basin system, western U.S.A. *Am. J. Sci.* 304, 105–168.
- Funiciello, F., Faccenna, C., Giardini, D., 2004. Flow in the evolution of subduction system: insights from 3-D laboratory experiments. *Geophys. J. Int.* 15, 1393–1407.
- Gurnis, M., Mueller, R.D., Moresi, L., 1998. Dynamics of Cretaceous vertical motion of Australia and the Australian–Antarctic discordance. *Science* 279, 1499–1504.
- Gurnis, M., S. Zahirovic, M. Turner, L. DiCaprio, S. Spasojevic, R. D. Müller, J. Boyden, M. Seton, V. C. Manea, and D. J. Bower, Plate reconstructions with continuously closing plates, *Computers & Geosciences*, submitted for publication.
- Humphreys, E., 1995. Post-Laramide removal of the Farallon slab, western United States. *Geology* 23, 987–990.
- Humphreys, E., 2009. Relation of flat subduction to magmatism and deformation in the western United States. *GSA Memoirs* 204, 85–98.
- Jadamec, M., Billen, M.L., 2010. Reconciling rapid 3-D mantle flow and surface plate motions near the eastern Alaska slab edge. *Nature* 465, 338–341.
- Lithgow-Bertelloni, C., Richards, M.A., 1998. The dynamics of Cenozoic and Mesozoic plate motions. *Rev. Geophys.* 36, 27–78.
- Liu, L., Gurnis, M., 2008. Simultaneous inversion of mantle properties and initial conditions using an adjoint of mantle convection. *J. of Geophys. Res.* 113, B08405.
- Liu, L., Spasojević, S., Gurnis, M., 2008. Reconstructing Farallon plate subduction beneath North America back to the Late Cretaceous. *Science* 322, 934–938.
- Liu, L., Gurnis, M., Seton, M., Saleeby, J., Müller, R.D., Jackson, J.M., 2010. The role of oceanic plateau subduction in the Laramide orogeny. *Nat. Geosci.* 3, 353–357.
- Long, M., Becker, T., 2010. Mantle dynamics and seismic anisotropy. *Earth Planet. Sci. Lett.* 297, 341–354.
- McQuarrie, N., Wernicke, B., 2005. An Animated Tectonic Reconstruction of Southwestern North America since 36 Ma, 1, 147–172.
- Morra, G., Regenauer-Lieb, K., Giardini, D., 2006. Curvature of oceanic arcs. *Geology* 34 (10), 877–880.
- Müller, R.D., Sdrolias, M., Gaina, C., Roest, W.R., 2008. Age, spreading rates and spreading asymmetry of the world's ocean crust. *Geochem. Geophys. Geosyst.* 9, Q04006. doi:[10.1029/2007GC001743](https://doi.org/10.1029/2007GC001743).
- Obrebski, M., Allen, R., Xue, M., Hung, S.-H., 2010. Slab–Plume Interaction Beneath the Pacific Northwest, 37. doi:[10.1029/2010GL043489](https://doi.org/10.1029/2010GL043489). L14305.
- Ozbench, M., Regenauer-Lieb, K., Stegman, D.R., Morra, G., Farrington, R., Hale, A., May, D.A., Freeman, J., Bourgouin, L., Mühlhaus, H., Moresi, L., 2008. A model comparison study of large-scale mantle–lithosphere dynamics driven by subduction. *Physics of the Earth and Planetary Interiors* 171, 224–234.
- Parsons, T., Thompson, G.A., Sleep, N.H., 1994. Mantle plume influence on Neogene uplift and extension of the U.S. western Cordillera? *Geology* 22, 83–86.
- Ribe, N.M., Stutzmann, E., Ren, Y., van der Hilst, R., 2007. Buckling instabilities of subducted lithosphere beneath the transition zone. *Earth Planet. Sci. Lett.* 254, 173–179.
- Ritsema, J., McNamara, A.K., Bull, A., 2007. Tomographic filtering of geodynamic models: implications for model interpretation and large-scale mantle structure. *J. Geophys. Res.* 112. doi:[10.1029/2006JB004566](https://doi.org/10.1029/2006JB004566).
- Roth, J., Fouch, M., James, D., Carlson, R., 2008. Three-dimensional seismic velocity structure of the northwestern United States. *Geophys. Res. Lett.* 35, L15304. doi:[10.1029/2008GL034669](https://doi.org/10.1029/2008GL034669).
- Royden, L.H., Husson, L., 2006. Trench motion, slab geometry and viscous stresses in subduction systems. *Geophys. J. Int.* 167, 881–905.
- Schmandt, B., Humphreys, E., 2010. Complex subduction and small-scale convection revealed by body-wave tomography of the western United States upper mantle. *Earth Planet. Sci. Lett.* doi:[10.1016/j.epsl.2010.06.047](https://doi.org/10.1016/j.epsl.2010.06.047).
- Sigloch, K., McQuarrie, N., Nolet, G., 2008. Two-stage subduction history under North America inferred from multiple-frequency tomography. *Nature Geosci.* 1, 458–462.
- Sigloch, K., 2011. Mantle provinces under North America from multifrequency P wave tomography. *Geochem. Geophys. Geosyst.* 12. doi:[10.1029/2010GC003421](https://doi.org/10.1029/2010GC003421) Q02W08.
- Schellart, W.P., Freeman, J., Stegman, D.R., Moresi, L., May, D.A., 2007. Evolution and diversity of subduction zones controlled by slab width. *Nature* 446, 308–311.
- Schellart, W.P., Stegman, D.R., Farrington, R.J., Freeman, J., Moresi, L., 2010. Cenozoic tectonics of western North America controlled by evolving width of Farallon slab. *Science* 329, 316–319. doi:[10.1126/science.1190366](https://doi.org/10.1126/science.1190366).
- Schellart, W.P., 2004. Kinematics of subduction and subduction-induced flow in the upper mantle. *J. Geophys. Res.* 109 B07401.
- Schmeling, H., Babeyko, A.Y., Enns, A., Faccenna, C., Funiciello, F., Geryad, T., Golabek, G.J., Grigull, S., Kaus, B.J.P., Morra, G., Schmalholz, S.M., van Hunen, J., 2008. A benchmark comparison of spontaneous subduction models—towards a free surface. *Phy. Earth Planet. Int.* 171, 198–223.
- Spasojevic, S., Liu, L., Gurnis, M., 2009. Adjoint models of mantle convection with seismic, plate motion, and stratigraphic constraints. *North America since the Late Cretaceous: Geochem. Geophys. Geosyst.* 10, Q05W02. doi:[10.1029/2008GC002345](https://doi.org/10.1029/2008GC002345).
- Stadler, G., Gurnis, M., Burstedde, C., Wilcox, L.C., Alisic, L., Ghattas, O., 2010. The dynamics of plate tectonics and mantle flow: from local to global scales. *Science* 329, 1033–1038.
- Stegman, D.R., Freeman, J., Schellart, W.P., Moresi, L.-N., May, D.A., 2006. Influence of trench width on subduction hinge retreat rates in 3-D models of slab. *Geochem. Geophys. Geosyst.* 7, Q03012.
- Stegman, D.R., Schellart, W.P., Freeman, J., 2010a. Competing influences of plate width and far-field boundary conditions on trench migration and morphology of subducted slabs in the upper mantle. *Tectonophysics* 483, 46–57. doi:[10.1016/j.tecto.2009.08.026](https://doi.org/10.1016/j.tecto.2009.08.026).
- Stegman, D.R., Farrington, R., Capitanio, F.A., Schellart, W.P., 2010b. A regime diagram for subduction styles from 3-D numerical models of free subduction. *Tectonophysics* 483, 29–45. doi:[10.1016/j.tecto.2009.08.041](https://doi.org/10.1016/j.tecto.2009.08.041).
- Tan, E., Gurnis, M., Han, L., 2002. Slabs in the lower mantle and their modulation of plume formation 3, 1067. doi:[10.1029/2001GC000238](https://doi.org/10.1029/2001GC000238).
- Tian, Y., Zhou, Y., Sigloch, K., Nolet, G., Laske, G., 2011. Structure of North American mantle constrained by simultaneous inversion of multiple-frequency SH, SS, and Love waves. *J. Geophys. Res.* 116, B02307. doi:[10.1029/2010JB007704](https://doi.org/10.1029/2010JB007704).
- West, J.D., Fouch, M.J., Roth, J.B., Elkins-Tanton, L.T., 2009. Vertical mantle flow associated with a lithospheric drip beneath the Great Basin. *Nat. Geosci.* 2, 439–444.
- Zandt, G., Humphreys, E., 2008. Toroidal mantle flow through the western U.S. slab window. *Geology* 36, 295–298.
- Zhong, S., Zuber, M.T., Moresi, L.N., Gurnis, M., 2000. The role of temperature-dependent viscosity and surface plates in spherical shell models of mantle convection. *J. Geophys. Res.* 105, 11,063–11,082.